The Effect of Loading Mode on Hydrogen Embrittlement

C. ST. JOHN AND W. W. GERBERICH

Hydrogen embrittlement is shown to occur very easily in notched-round bars under opening mode *I* (tension) but not under antiplane shear mode *III* (torsion). The stress tensor invariants under mode *I*, *II*, and *III* loadings and how these affect interstitial diffusion are discussed. It is suggested that long range diffusion of hydrogen down orthogonal trajectories to the vicinity of the crack tip, which can occur under mode *I* but not mode *III*, is a key part of any hydrogen embrittlement mechanism. This premise was evaluated with AISI 4340 steel heat treated to ultrahigh strength levels. It was found that an initial mode *I* stress intensity level of 17,000 psi-in.$^{1/2}$ produced failure in several minutes. Mode *III* stress intensity levels three times this produced no crack initiation in 300 min. Further analysis of the time-dependent hydrogen concentrating effect utilized a stress wave emission technique. This produced plausible critical hydrogen concentrations even though the present elastic analysis is a first order approximation of the stress field.

THE problem of hydrogen embrittlement has generated considerable discussion regarding the exact mechanism(s) involved.[1,2] There does appear to be some agreement however on the role that the localized stress fields in the crack tip region play in all three currently held mechanisms; which is, to create hydrogen concentrations via "up-hill" diffusion that can be considerably higher than those away from the crack tip. The concept of an elastic interaction between the volumetric component of a crack tip stress tensor and the dilation associated with an interstitial hydrogen atom has been discussed before.[3] More recently,[4] an analysis of the hydrostatic pressure field of a crack under mode *I* loading coupled with Fick's first law has yielded steady state solute concentration gradients similar to those obtained directly from thermodynamics.[5]

$$C = C_0 e^{u/kT}/(1 - C_0 + C_0 e^{u/kT}) \simeq C_0 e^{u/kT} \quad \text{for } C_0 \text{ small} \qquad [1]$$

where u is the interaction energy between the crack tip pressure field and hydrogen atom dilation, and C_0 is the homogeneous hydrogen solid solution concentration far from the crack tip.

The stress tensor associated with the tip of a mathematically sharp crack in an isotropic continuum is of the following form in polar coordinates:

$$\sigma_{ij} = \frac{K_k}{\sqrt{2\pi r}} f_{ijk}(\theta/2) \qquad [2]$$

where K_k is the stress intensity factor for a particular loading mode, k.

The hydrostatic pressure is defined in terms of the stress tensor invariant, σ_{ii} (where the usual summation convention is assumed),

$$-P = \frac{\sigma_{ii}}{3} \qquad [3]$$

On examining the $f_{ij}(\theta/2)$ for each of the three independent loading modes it can be easily shown that,*

*See Appendix.

$$\begin{aligned} -P &= A \cos(\theta/2) && \text{mode } I \\ -P &= -A \sin(\theta/2) && \text{mode } II \\ -P &= 0 && \text{mode } III \end{aligned} \qquad [4]$$

where $A \equiv \frac{2K_k}{3\sqrt{2\pi r}}$ for the plane stress condition

$\equiv \frac{2K_k}{3\sqrt{2\pi r}}(1+\nu)$ for the plane strain condition.

Rearranging the above relationships, the isopressure curves for each crack loading mode are of the form,

$$\begin{aligned} r &= B \cos^2(\theta/2) && \text{mode } I \\ r &= -B \sin^2(\theta/2) && \text{mode } II \end{aligned} \qquad [5]$$

No volumetric term for mode *III*.

The orthogonal trajectories or gradients to the isopressure curves can be derived directly and represent the hydrogen diffusion paths, in the absence of any plasticity, towards regions of increasing negative pressure. In polar coordinates, the pressure gradient curves for each loading mode are

$$\begin{aligned} r &= C \sin^2(\theta/2) && \text{mode } I \\ r &= -C \cos^2(\theta/2) && \text{mode } II \end{aligned} \qquad [6]$$

No volumetric term for mode *III*.

The above two sets of relations show a symmetry between mode *I* and mode *II* in that the isopressure curves of one mode are the gradient curves of the other mode and vice versa, as is shown in Fig. 1.

The most important point to be derived from the hydrostatic pressure analysis of the crack tip region is the hydrogen concentrating effect of the gradient lines in modes *I* and *II* and the absence of this effect in mode *III*. One would expect therefore that hydrogen containing steels would be much more susceptible to hydrogen embrittlement while loaded in either modes *I* or *II* than in mode *III*. The object of the experimental portion of this work was to compare, in a cursory fashion, the effect of loading mode on the susceptibility of a high strength steel to hydrogen embrittlement.

C. ST. JOHN and W. W. GERBERICH, formerly Graduate Student and Lecturer, respectively, University of California, Berkeley, are now Research Scientist, Centre des Materiaux de l'Ecole des Mines, Corbeil-Essone, France and Associate Professor, University of Minnesota, Minneapolis, Minn. 55455.

Manuscript submitted January 24, 1972.

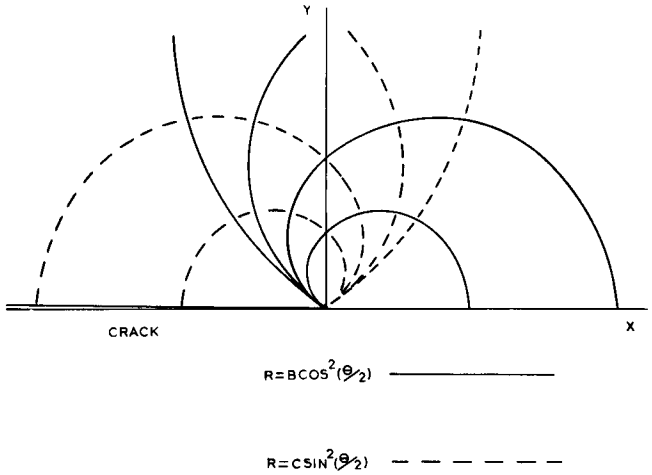

Fig. 1—Isopressure contours and gradients for a crack loaded in modes *I* or *II*, $0 < \theta/2 < 90$ deg.

MATERIALS AND PROCEDURE

A commercial high strength steel, SAE-AISI 4340, was employed in this study after being austenitized for 1 h at 1550°F, oil quenched, and tempered for 4 h at 550°F. The hydrogenated specimens were cathodically charged in a 4 pct sulfuric acid solution poisoned with yellow phosphorus which, according to another study,[6] yields a predictable relationship between hydrogen content and applied current density. In this case, a current density of 0.0003 amp/sq in. for 24 h should have resulted in 3.8 ppm of hydrogen in solid solution. Immediately after cathodic charging, the specimens were transported while immersed in alcohol and dry ice to the fracture testing equipment and loaded. All testing was at room temperature.

The most convenient mode *III* loading arrangement is the torsion of notched round bars. For comparison purposes both mode *I* and mode *III* tests were carried out on 60 deg V-notched round specimens with a 0.750 in. uniform diameter and a 0.500 in. diam at the V-notch root. The notch root radii were determined to be close to 0.003 in. except for one specimen which had a radius of 0.004 in. The specimens were not precracked via the standard fatigue procedure because of the difficulty in obtaining a uniform crack penetration in notched round configurations. The mode *I* fracture testing of hydrogenated specimens consisted of loading to preselected tensile stresses and holding for various times while simultaneously monitoring for stress wave emissions (SWE).[7] The mode *III* hydrogenated specimens were tested in basically the same manner as the mode *I* counterparts except that the loading was in torsion and the stress wave emission monitoring was not available.

It would have been best to evaluate all three loading modes. However, it was desirable to use the same specimen configuration so that charging conditions and the corresponding hydrogen distributions were identical. Since it is difficult if not impossible to achieve a mode *II* test with a circumferential notched round, we confined the present study to mode *I* and *III* tests.

RESULTS AND DISCUSSION

The critical loads and stress intensities for failure along with loading histories are summarized in Table I.

Table I. Critical Loads, Stress Intensities, and Hold Times for Mode *I* and Mode *III* Testing

Hydrogen Content	Loading History	Mode *I* P_{IC}, lb.	Mode *I* K^{+}_{IC}, psi-in.$^{1/2}$	Mode *III* T_{IIIC}, in.-lb.	Mode *III* K^{+}_{IIIC}, psi-in.$^{1/2}$
without hydrogen charging	All uncharged specimens loaded directly to failure	57,000 (two tests)	115,000	5075	63,500
with hydrogen charging	(*a*) 20 min at 8,240 lb. with no SWE*; failure after 2 min at 9250 lb. with many ~3100 SWE	9250	26,200		
	(*b*) 20 min at 2000 in.-lb., rising torque to failure			4200	52,500
	(*c*) 330 min at 3600 in.-lb., rising torque to failure			4380	54,700

+Except for specimen (*a*) which failed from a sharp crack, the K_{IC} and K_{IIIC} values are apparent ones in the sense that failure was initiated from a relatively blunt notch. Nevertheless, the qualitative comparisons of cracking under these widely varying degrees of stress intensification is illustrative.

*Stress wave emission.

The results are arranged according to hydrogen content and loading mode.

Specimen (*a*), hydrogen-charged and loaded in mode *I*, exhibited slow crack propagation to eventual catastrophic failure at a critical stress intensity that is typical of ultrahigh strength steel.[8] The slow crack growth was followed during the test by monitoring the stress wave emissions (SWE). In Fig. 2(*a*), the fracture surface shows the initial slow crack growth region and the subsequent rapid growth across the remaining segment after K_{IC} had been attained. The K_{IC} was estimated from the following relationship,[9]

$$K_I = \frac{P}{D^{3/2}}\left[1.72\frac{D}{d} - 1.27\right] \qquad [7]$$

where P is the applied load,
D is the diameter of uniform cross-section,
d is the diameter of reduced cross-section, which is this case was estimated by the average diameter of the uncracked segment at the onset of rapid crack growth.

Two static torque loads were examined in the mode *III*, hydrogenated specimens. The first trial, specimen (*b*), utilized an equivalent stress intensity that proved to be fatal for specimen (*a*). The mode *III* stress intensity formula employed was obtained from a finite element analysis;[10]

$$K_{III} = \frac{YT}{(d/2)^{2.5}} \qquad [8]$$

where Y is a constant for any particular (d/D) and
T is the applied torque.

Specimen (*b*) showed no evidence of slow crack growth after 20 min at an equivalent stress intensity that provided failure in 2 min under mode *I* loading. The torque was then slowly increased until a slow ductile failure ensued, the resulting ductile fracture surface is shown in Fig. 2(*c*). Specimen (*c*) was loaded at 80 pct of the torque that induced plastic shear failure in spe-

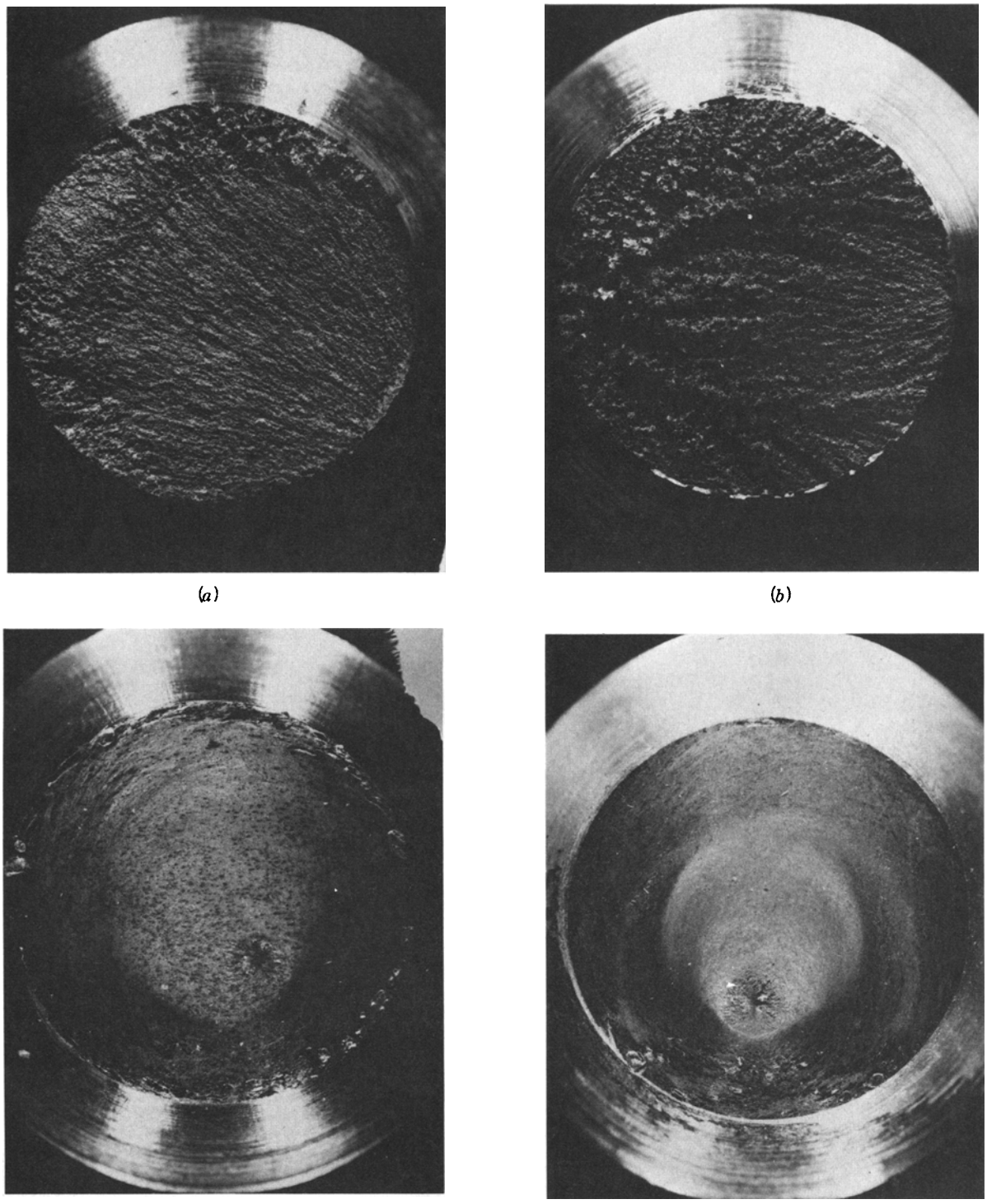

Fig. 2—Mode *I* fracture surfaces: (*a*) hydrogen charged, (*b*) control; Mode *III* fracture surfaces: (*c*) hydrogen charged, (*d*) control.

cimen (*b*). This was held for 330 min with no evidence of crack growth. The torque was then slowly raised to specimen failure that occurred in the same manner and at approximately the same load as for specimen (*b*). The fracture surface for specimen (*c*) was indistinguishable from specimen (*b*).

Three uncharged specimens were loaded directly to failure, two in mode *I* and one in mode *III*. No evidence of slow crack growth at low stress intensities was observed on the fracture surfaces of any of these control specimens as is shown in Figs. 2(*b*) and 2(*d*). The load necessary to induce crack initiation on mode *I* was approximately 450 pct greater than that for the hydrogenated material. In mode *III*, however, the critical torque was only 17 pct greater than that obtained from the charged specimens. This difference between the charged and uncharged specimens loaded in mode *III* may be explained by the anomalously large notch root

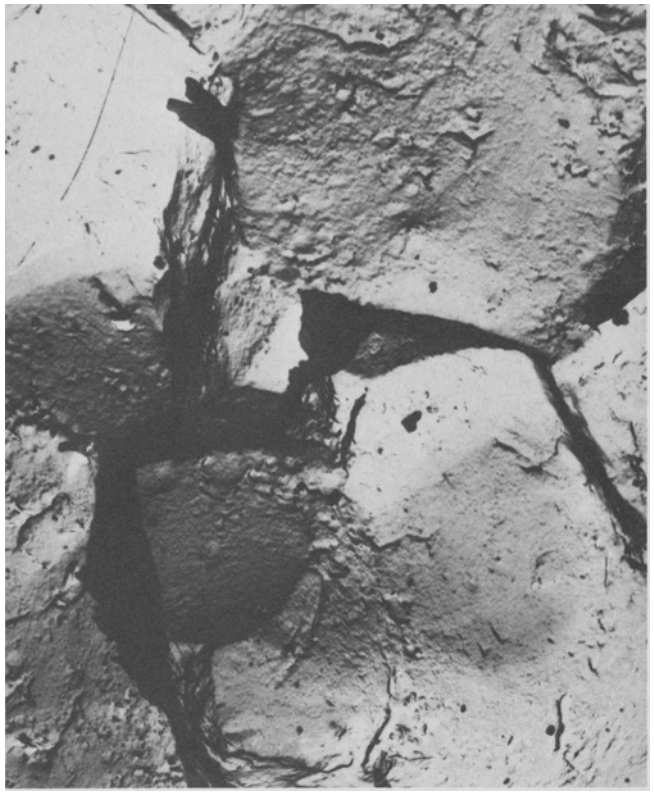

(a)

(b)

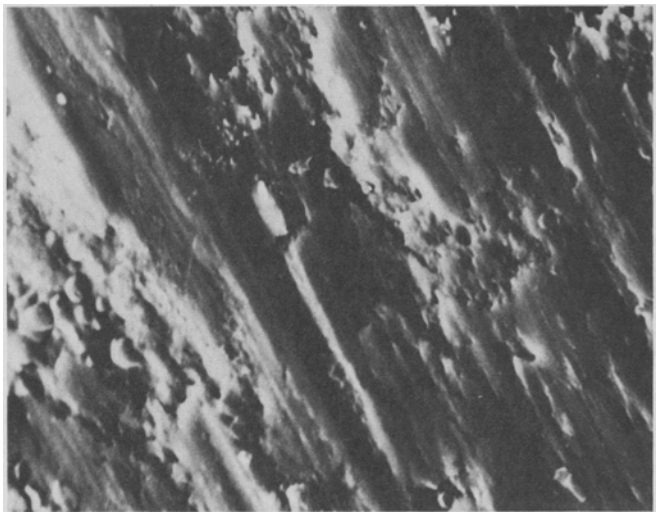

(c)

Fig. 3—Fractography of mode *I*: (*a*) replica of hydrogen charged sample; (*b*) scanning electron microscopy of hydrogen charged sample: Fractography of mode *III*: (*c*) scanning electron microscopy typical of hydrogen charged and control samples.

radius of the control specimen which would decrease the stress concentration. The fracture surfaces for charged and uncharged mode *III* specimens were identical. The difference between mode *I* and *III* fracture surfaces, for the specimen with prior hydrogenation, are more clearly illustrated by scanning and replica electron fractography of the fracture surfaces in Fig. 3. Here it is seen that the slow crack growth process in mode *I* is definitely an intergranular fracture process as may be associated with hydrogen embrittlement. On the other hand, scanning of the outer periphery of the crack surfaces from the mode *III* specimen only revealed the morphology shown in Fig. 3(*c*) for both charged and uncharged specimens. This would be characteristic of a ductile fracture where the surfaces had rubbed together.

Thus, one may conclude that both mechanical test data and fracture surface observations verify the hydrogen embrittlement mechanism under mode *I* loading but not under mode *III*. The main reason would appear to be the difference in the stress field interaction with hydrogen. The fact that mode *III* did not produce hydrogen embrittlement should be put in perspective since some interaction of the hydrogen with the stress field is possible. For example, if hydrogen in solution produces a tetragonal distortion, the nonisotropic stress field can interact with the elastic shear stress as pointed out by Li, Oriani, and Darken,[11] for carbon in α-Fe. However, this would probably be a second-order effect as compared to the interaction with the dilitant field of mode *I*.

Considering the SWE data from specimen (*a*) tested in mode *I*, 3100 SWE were detected during the slow crack growth period. A small portion of oscillograph playback in Fig. 4 indicates the discontinuous nature of the embrittlement process. These were associated with a total crack growth area of 0.061 in.^{2} so that on the average, each SWE is associated with an area of 2×10^{-5} in.^{2} or a linear dimension of about 0.0045 in.

I TIMING LINE = 0·5 SECONDS

Fig. 4—A few of the SWE recorded during the slow crack growth stage of specimen (*a*) under mode *I* loading.

If the distance over which the hydrogen concentrates and nucleates fracture is on the same order of magnitude as this fracture region, then the preceding equations may be utilized to estimate the amount of hydrogen concentrating in this region. Using the thermodynamic equivalent to Eq. [19] in Ref. 4, the equilibrium concentration is given by

$$C = C_0 \exp\left\{\frac{2(1+\nu)\overline{V}_H K}{3\sqrt{2\pi r}\,RT}\right\} \qquad [9]$$

Using the average stress intensity during slow crack growth of 21,400 psi-in.$^{1/2}$ (2.38×10^9 dyne-cm$^{-3/2}$), the linear dimension of 0.0045 in. (0.0115 cm), and the value of 2.0 cm^3/g-atom for the partial molal volume of hydrogen in iron for $\overline{V}_H$,[3] one calculates at room temperature that $C = 1.9C_0$. If the previously estimated value of 3.8 ppm H is assumed, then $C \simeq 7.2$ ppm H which is very close to other estimates[11] for the critical hydrogen concentration. Of course, one must take into consideration that a) with the short time involved equilibrium probably was not achieved and b) this is a purely elastic solution and the gradient due to the plastic zone was not considered. Nevertheless, since the value predicted is sufficiently close to what one might expect, this approach merits further consideration.

SUMMARY

The comparative tests performed on hydrogen charged and control specimens give strong evidence that high strength steel loaded in the mode *III* configuration is insensitive to hydrogen embrittlement when compared to mode *I* loading. An interpretation of these results is that the hydrostatic pressure fields associated with mode *I* stress concentrations raise the hydrogen solid solution concentrations to critical values that are necessary to initiate slow crack growth by any one of the currently held mechanisms.

ACKNOWLEDGMENTS

This work was supported by the United States Atomic Energy Commission. The authors would like to thank Y. T. Chen and J. Cohen for assistance with electron fractography and scanning electron microscopy.

APPENDIX

The stress fields about cracks under various types of loading have been discussed at great length,* but will be reiterated here to assist those unfamiliar with fracture mechanics analyses. In particular, the stress tensor invariant associated with the driving force for long range hydrogen diffusion at the tip of a crack is determined. Two mathematical extremes are considered, plane stress where $\sigma_z = 0$ and plane strain where $\epsilon_z = 0$ and hence $\sigma_z = \nu(\sigma_x + \sigma_y)$.

For the opening Mode *I*:

In terms of polar coordinates, r, θ, the stresses are a function of position and the magnitude of the stress intensity factor, K_I.

$$\sigma_x = \frac{K_I}{(2\pi r)^{1/2}} \cos\frac{\theta}{2}\left[1 - \sin\frac{\theta}{2}\sin\frac{3\theta}{2}\right]$$

$$\sigma_y = \frac{K_I}{(2\pi r)^{1/2}} \cos\frac{\theta}{2}\left[1 + \sin\frac{\theta}{2}\sin\frac{3\theta}{2}\right] \qquad [A\text{-}1]$$

$$\tau_{xy} = \frac{K}{(2\pi r)^{1/2}} \sin\frac{\theta}{2}\cos\frac{\theta}{2}\cos\frac{3\theta}{2}$$

$$\sigma_z = 0 \text{ for plane stress}$$

$$\sigma_z = \nu(\sigma_x + \sigma_y) \text{ for plane strain}$$

$$\tau_{xz} = \tau_{yz} = 0$$

Determination of the pressure is simplified by recognizing that

$$\sigma_1 = \frac{\sigma_x + \sigma_y}{2} + \tau_{max}$$

$$\sigma_2 = \frac{\sigma_x + \sigma_y}{2} - \tau_{max} \qquad [A\text{-}2]$$

$$\sigma_3 = \nu(\sigma_x + \sigma_y).$$

Thus, for plane stress, where $\sigma_3 = 0$,

$$-P = \frac{\sigma_1 + \sigma_2 + \sigma_3}{3} = \frac{\sigma_x + \sigma_y}{3}$$

and for plane strain,

$$-P = \frac{(1+\nu)(\sigma_x + \sigma_y)}{3} \qquad [A\text{-}3]$$

Combining Eqs. [A-1] and [A-3] give

$$-P = \frac{2K_I}{3(2\pi r)^{1/2}} \cos\left(\frac{\theta}{2}\right) \text{ for plane stress}$$

$$-P = \frac{2(1+\nu)K_I}{3(2\pi r)^{1/2}} \cos\left(\frac{\theta}{2}\right) \text{ for plane strain} \qquad [A\text{-}4]$$

as given in Eq. [4].

For the in-plane shear Mode *II*:

$$\sigma_x = -\frac{K_{II}}{(2\pi r)^{1/2}} \sin\frac{\theta}{2}\left[2 + \cos\frac{\theta}{2}\cos\frac{3\theta}{2}\right]$$

$$\sigma_y = \frac{K_{II}}{(2\pi r)^{1/2}} \sin\frac{\theta}{2}\cos\frac{\theta}{2}\cos\frac{3\theta}{2}$$

$$\tau_{xy} = \frac{K_{II}}{(2\pi r)^{1/2}} \cos\frac{\theta}{2}\left[1 - \sin\frac{\theta}{2}\sin\frac{3\theta}{2}\right] \qquad [A\text{-}5]$$

$$\sigma_z = 0 \text{ for plane stress}$$

$$\sigma_z = \nu(\sigma_x + \sigma_y) \text{ for plane strain}$$

$$\tau_{xz} = \tau_{yz} = 0$$

Combining Eqs. [A-1] and [A-5] give

$$-P = -\frac{2K_{II}}{3(2\pi r)^{1/2}} \sin\left(\frac{\theta}{2}\right) \text{ for plane stress} \qquad [A\text{-}6]$$

*For example, see Paris and Sih[13] for a discussion of both stress analysis and a description of the various types of loading modes.

$$-P = -\frac{2(1+\nu)K_{II}}{3(2\pi r)^{1/2}} \sin\left(\frac{\theta}{2}\right) \text{ for plane strain}$$

also given in Eq. [4].

For the antiplane shear Mode *III*:

$$\sigma_x = \sigma_y = \sigma_z = \tau_{xy} = 0$$

$$\tau_{xy} = \frac{-K_{III}}{(2\pi r)^{1/2}} \sin\frac{\theta}{2}; \quad \tau_{yz} = \frac{K_{III}}{(2\pi r)^{1/2}} \cos\frac{\theta}{2}$$

$$-P = 0$$

REFERENCES

1. D. P. Williams and H. G. Nelson: *Met. Trans.*, 1971, vol. 2, p. 1987.
2. C. F. Barth and E. A. Steigerwald: *Met. Trans.*, 1971, vol. 2, p. 1988.
3. R. A. Oriani: *Fundamental Aspects of Stress Corrosion Cracking*, p. 32, National Association of Corrosion Engineers, Houston, 1969.
4. H. W. Liu: *J. Basic Eng., ASME*, 1970, vol. 92, p. 633.
5. D. McLean: *Grain Boundaries in Metals*, p. 118, Oxford at the Clarendon Press, 1957.
6. C. F. Barth and E. A. Steigerwald: *Met. Trans.*, 1970, vol. 1, p. 3451.
7. C. E. Hartbower, W. W. Gerberich, and P. P. Crimmins: *Welding J. Res. Supp.*, 1968, vol. 47, no. 1, p. 1s.
8. A. J. Baker, F. J. Lauta, and R. P. Wei: *Amer. Soc. Test. Mater. Special Tech. Publ.* 370, 1965, p. 3.
9. W. F. Brown and J. E. Srawley: *Amer. Soc. Test. Mater. Special Tech. Publ.* 410, 1966.
10. W. K. Wilson, W. G. Clark, Jr., and E. T. Wessel: *Fracture Mechanics Technology for Combined Loading and Low-To-Intermediate Strength Metals*, Westinghouse Research Lab., Contract DAAE 07-67-C-4021, November 1968.
11. J. C. M. Li, R. A. Oriani, and L. S. Darken: *Z. Physik. Chem.*, 1966, vol. 49, p. 271.
12. R. A. Oriani: *Fundamental Aspects of Stress Corrosion Cracking*, p. 49, National Assoc. of Corrosion Engineers, Houston, 1969; see also W. W. Gerberich and C. E. Hartbower, p. 426; M. Smialowski, p. 463.
13. P. C. Paris and G. C. Sih: *Amer. Soc. Test. Mater. Special Tech. Publ.* 381, 1965, p. 30.